



## Evaluating the seasonal effects of building form and street view indicators on street-level land surface temperature using random forest regression

Keyan Chen <sup>a,b</sup>, Meng Tian <sup>a,b,c</sup>, Jianfeng Zhang <sup>a,b</sup>, Xuesong Xu <sup>a,b,c</sup>, Lei Yuan <sup>a,b,\*</sup>

<sup>a</sup> School of Architecture and Urban Planning, Shenzhen University, Shenzhen, 518060, China

<sup>b</sup> Shenzhen Key Laboratory for Optimizing Design of Built Environment, Shenzhen University, Shenzhen, 518060, China

<sup>c</sup> The Institute of Architecture Design & Research, Shenzhen University, Shenzhen, 518060, China



### ARTICLE INFO

#### Keywords:

Urban morphology  
Land surface temperature  
Thermal environment  
Building form  
Street view image  
Random forest

### ABSTRACT

Current studies of the influence of urban morphology indicators on land surface temperature (LST) usually focus on administrative or grid-based research units, and the limited inclusion of similar indicators easily occurs due to multicollinearity. This study implements Random Forest (RF) models with multi-source data, to study the relative importance and marginal effects of eight building form indicators as well as six street view indicators on street-level LST across all four seasons for Shenzhen, China. Our results show that the RF models explained 79.56%, 79.07%, 76.42%, and 64.74% of the LST variations in the spring, summer, autumn and winter, respectively. The building view factor (BVF) and green view index (GVI) were identified as the two most important indicators across all seasons. However, BVF was the dominant indicator in the spring and summer, and GVI played more significant roles in the autumn and winter. The relative importance of building density (BD), average building height (BH), standard deviation of building height (BH\_SD) and sky view factor (SVF) showed noticeable variations with the seasons as well. The trends of marginal effects remained stable for each indicator across the four seasons. BVF, BD and SVF had warming effects in each season, while GVI, BH and BH\_SD had cooling effects in each season. These findings contribute to our understanding of the relationship between urban morphology indicators and LST and provide valuable design suggestions for improving urban thermal environment, especially in high-density cities.

### 1. Introduction

Rapid urbanization has led to significant changes in land use and land cover. With artificial structures and impermeable surfaces replacing natural features such as vegetation, water bodies, and soil, these transformations have resulted in significant alterations to the urban biophysical environment and climate [1]. The widely studied Urban Heat Island (UHI) effect refers to the phenomenon where the air temperature (AT) and land surface temperature (LST) in urban areas are higher than those in surrounding rural areas [2]. This effect can result in increased building energy consumption during summer [3], higher water consumption [4], air pollution [5], intensified heat waves [6] and reduced outdoor thermal comfort [7]. Excessive heat also increases health risks and even mortality rates among urban residents [8]. A study based on 13,115 cities worldwide revealed that around 1.7 billion people are exposed to extreme heat conditions [9]. This exposure risk highlights the urgent need to identify the factors and mechanisms that

influence the urban thermal environment. It is essential to optimize urban planning and architectural designs to mitigate the impacts of extreme heat and improve urban resilience.

Compared to the limited density of AT monitoring stations, LST retrieved through remote sensing satellites offers the advantages of convenience, large-scale coverage and high accuracy [10]. LST has been widely used in studies related to the urban thermal environment and its influencing factors [11–13]. Urban morphology is one such factor, and appropriate urban morphology design can significantly mitigate the UHI effect [14,15]. The morphology, arrangement and density of buildings affect the ventilation, radiation and solar exposure at the block and city scale, and thus influencing the accumulation or dissipation of urban heat [16]. The two-dimensional (2D) indicators of building form, such as building density (BD) and building coverage ratio (BCR), describe the building compactness, and numerous studies have demonstrated the warming effects of BD and BCR on LST [16–18]. Common three-dimensional (3D) building form indicators include building height

\* Corresponding author.

E-mail address: [yuanlei@szu.edu.cn](mailto:yuanlei@szu.edu.cn) (L. Yuan).

(BH), building volume (BV), and floor area ratio (FAR) [11,19]. In many studies, the influences of 3D indicators on LST are more complex and uncertain compared to 2D indicators, which are also affected by climatic zones and the built environment at the land surface [19]. The standard deviation of building height (BH\_SD) and the standard deviation of building volume (BV\_SD) characterize the variations in building height and volume respectively, and thus influence the thermal balance and ventilation effects in cities [20]. Some certain building form indicators used in aerodynamics and urban meteorology, such as the frontal area index (FAI), have been shown to influence local microclimates and wind environment [21], but their impact on LST requires further investigation. Furthermore, several studies have found that LST exhibits seasonal variations in response to various driving factors [20,22,23].

Past studies on LST have primarily investigated the impact of urban morphology on LST at the scales of blocks, planning management units and grids [16,24,25]. Streets, as integral components of public spaces, have been the objects of research in various aspects, such as solar radiation [26], noise pollution [27], and urban vitality assessment [28]. However, studies that specifically focus on the LST at street-level have been relatively limited. Streets are often surrounded by elements such as the sky, buildings and green vegetation, and thus creating a complex thermal environment to which urban residents and non-motorized transportation users are directly exposed [26]. It is necessary to study the distribution of LST on streets and its influencing factors. Traditional urban thermal environment studies have relied on data from remote sensing satellites [13]. However, due to the top-down data acquisition method of remote sensing satellites, the semantic structures at the vertical scale of the city are neglected [29]. Street view images (SVIs) with geotags collected by mapping service providers such as Google, Baidu, and Tencent have provided a vast and novel data source for studying the urban environment at street-level. Although the purchase of application programming interface (API) keys is usually required for these map platforms, their advantages in providing panoramic view provision, comprehensive spatial coverage and high accuracy of photo position have contributed to their popularity in many studies [26,28,30]. Some open-source platforms like Mapillary and KartaView also provide massive geotagged SVIs that are uploaded by users and can be used freely, the images from these crowdsourcing platforms were taken from different devices, making it difficult to ensure the quality of the images and to maintain the perspective in photographic composition [31]. Combining with deep learning-based semantic segmentation models, SVI enables the extraction of many indicators that traditionally require on-site measurements. For example, the green view index (GVI) derived from SVIs has been shown to capture vegetation in urban centers better compared to the normalized difference vegetation index (NDVI) obtained from remote sensing [32]. The building view factor (BVF) is usually used to quantify the impact of buildings on the urban radiation balance [33]. The sky view factor (SVF) is used to assess the openness of streets, which affects the amount of radiation received [34]. SVF is commonly calculated using building data [16,23,35], but this method overlooks the obstruction caused by vegetation and other obstacles in the actual environment, which leads to the deviations from the true values and uncertainty in the results [36]. These methods based on SVIs and semantic segmentation methods do not rely on 3D city models, and they have the advantages of lower costs and better accuracy.

Multiple linear regression, geographically weighted regression, and spatial autoregression have been widely used to identify the relationships between various influencing factors and LST [11,24,37]. However, these methods can only identify positive or negative correlations; they cannot determine the dynamic relationship between the variables and LST [16]. Machine learning models do not require specific assumptions about the mapping functions and can define the relations more freely and flexibly [35]. Thus, tree-based machine learning models, including Boosted Regression Tree (BRT), eXtreme Gradient Boosting (XGBoost) and Random Forest (RF), have been used to explore the driving factors of LST in recent years [38–43]. In a comparative study by Logan et al. that

compared several linear and machine learning models, RF was also shown to be the most effective model [22]. RF is an ensemble machine learning algorithm that is robust to multicollinearity and suitable for regression and classification tasks with large datasets [44]. Some interpretation and visualization tools are available to help understand the essence of RF models [45]. The relative importance is commonly used to quantify the expected fraction that each indicator contributes to, and the Partial Dependence Plot (PDP) is used to show the marginal effects of LST with one indicator by marginalizing over the values of all other indicators [20,23,42].

In summary, although a considerable number of studies have investigated the correlations between LST and urban morphology, there are still some limitations. Firstly, remote sensing data ignores many constituent elements of street and urban built environment. Secondly, there is limited research on the driving mechanism of urban morphology on street-level LST. Moreover, the variations in seasons and statistical scales can affect analysis results. Finally, previous studies that focused on the positive and negative correlations between urban form and LST usually lack discussions on their marginal effects. To fill these research gaps, we select Shenzhen, China as research area and aim to quantify the relationship between seasonal LST and urban morphology (including street view and building form) using multi-source data and RF regression. To begin with, we reveal the spatial distributions of seasonal LST and the urban morphology indicators. Then we investigate the seasonal relative importance of urban morphology in LST variations and examine the marginal effects of major indicators in four seasons. Lastly, the suggestions for urban planning and management to mitigate urban thermal environment are discussed. The findings of this study therefore contribute to a better understanding of the influence mechanisms of urban morphology on urban thermal environment and allow urban planners to develop effective strategies for mitigating the UHI effect through thoughtful building design and urban planning.

## 2. Study area and data

### 2.1. Study area

Shenzhen is located in the southeastern part of Guangdong Province, China ( $113^{\circ}43' - 114^{\circ}38'E$ ,  $22^{\circ}24' - 22^{\circ}52'N$ ). It covers a total area of  $1997 \text{ km}^2$  with a population of 17.68 million people by 2022 (<http://tjj.sz.gov.cn/>). The subtropical maritime monsoon climate in Shenzhen makes it hot and humid. The annual average temperature is  $24.0^{\circ}\text{C}$ , and the annual precipitation is 1822.5 mm, with an average relative humidity of 74% (<http://tjj.sz.gov.cn/>). Shenzhen consists of ten administrative districts (Fig. 1). A large portion of the city has been developed over the past four decades [46]. As a typical high-density city, the extensive development has led to a rapid increase in artificial surfaces that exacerbated the UHI [47]. In addition, Shenzhen has not only dense urban villages but also 367 high-rise buildings over 150 m (<https://www.skyscrapercenter.com/cities/>), which causes significant variations in building forms. The diverse and complex features of building density, form, height and spatial configuration exhibit obvious spatial heterogeneity [48], making it an ideal region for exploring the effects of urban morphology on LST.

### 2.2. Data

To cover the entire area of Shenzhen, two satellite images should be used for LST retrieval. The Landsat 8–9 satellites consist of 11 spectral bands, of which the band 10 was used for retrieving LST. We filtered the dataset of Landsat 8–9 OLI/TIRS C2 L1 with the cloud cover being less than 10% from the website of the United States Geological Survey (USGS) (<https://earthexplorer.usgs.gov/>). According to the historical monthly average temperature in Shenzhen over the past 34 years [47], the satellite images of early April, early September, late October and late December were chosen to retrieve the LST of spring, summer, autumn

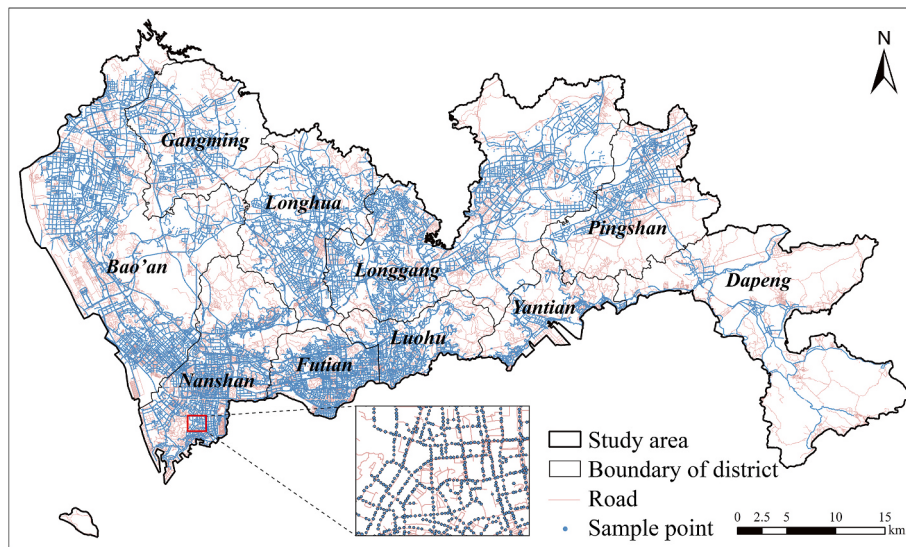


**Fig. 1.** Visualization of the study area and the SVI sampling points.

and winter respectively. Given the influence of weather on LST, the collection dates for the satellite images were all sunny with calm or light winds (<http://weather.sz.gov.cn/>). Finally, a total of 8 Landsat images were selected as the data source for LST retrieval as shown in [Table 1](#).

The street network data of the study area was obtained from the OpenStreetMap (OSM) (<https://www.openstreetmap.org/>). The SVI sampling points were established along the road network at 50 m intervals following previous studies [26,49,50]. The visual range of SVI is usually more than 50 m [51], the intervals of 50 m we chose can ensure the continuity of the street view. Baidu is one of the largest street view providers in China, which has collected panoramic data on 652 cities across China, covering a total distance of 2.295 million kilometers by August 2023 (<https://quanjing.baidu.com/>). We first downloaded 92,391 SVIs covering the study area from Baidu Street View (<https://lbsyun.baidu.com/>) in August 2021. Then we manually removed 1803 obstructed images that were taken in tunnels or under overpasses to avoid bias in subsequent analysis. Finally, 90,588 panoramic SVIs with a resolution of  $4096 \times 1536$  pixels were obtained, covering the major roads in Shenzhen, as shown in [Fig. 1](#). A higher resolution would facilitate higher accuracy for semantic segmentation. The dataset of building was obtained from Baidu Map (<https://lbsyun.baidu.com/>) in 2021.

**Table 1**  
Data sources for remote sensing images.

Season	Sensor	Date	Local time	Path/Row	Cloud cover (%)	Air temperature (°C)
Spring	Landsat 9	2022/04/04	10:52:03	122/044	0.42	16.7–28.2
	Landsat 8	2022/04/05	10:45:26	121/044	0.11	17.9–30.2
Summer	Landsat 8	2022/09/03	10:52:22	122/044	0.45	27.2–34.3
	Landsat 9	2022/09/12	10:46:17	121/044	4.68	29.5–37.6
Autumn	Landsat 8	2022/10/21	10:52:26	122/044	1.96	23.1–32.7
	Landsat 8	2022/10/14	10:46:09	121/044	0.45	24.5–31.9
Winter	Landsat 8	2022/12/24	10:52:14	122/044	0.50	14.0–22.2
	Landsat 9	2022/12/25	10:46:04	121/044	0.09	13.7–22.4

### 3. Methods

The research framework, as shown in [Fig. 2](#), comprised four primary steps: (1) retrieving seasonal LST from Landsat images by RTE method; (2) calculating building form and street view indicators from 3D building dataset and SVI; (3) employing RF model to investigate the relationships between urban morphology and LST; (4) evaluating the impacts of urban morphology on LST through relative importance and PDP.

#### 3.1. Retrieval of land surface temperature

The LST was retrieved from the thermal infrared bands of the remote sensing images using the radiative transfer equation (RTE) method [52]. The RTE removes the atmospheric bias from the total thermal radiation observed by the satellite sensors, and then calculates surface thermal radiation intensity and LST [53]. The calculation steps are as follows [54]:

The apparent radiance  $L_\lambda$  received by the sensor can be calculated by:

$$L_\lambda = [\varepsilon B(T_S) + (1 - \varepsilon)L_\downarrow]\tau + L_\uparrow \quad (1)$$

where  $\varepsilon$  is land surface emissivity,  $T_S$  is the LST (K),  $B(T_S)$  is ground radiation,  $L_\downarrow$  is downwelling atmospheric radiation,  $L_\uparrow$  is upwelling atmospheric radiation,  $\tau$  is total atmospheric transmissivity between surface and sensor. The parameters  $L_\downarrow$ ,  $L_\uparrow$  and  $\tau$  are calculated using the NASA web-based tool (<https://atmcorr.gsfc.nasa.gov/>), and their results are shown in Appendix [Table A.1](#).  $B(T_S)$  can be expressed as:

$$B(T_S) = [L_\downarrow - L_\uparrow - \tau(1 - \varepsilon)L_\downarrow]/\varepsilon\tau \quad (2)$$

Thus, LST can be calculated by:

$$T_S = K_2/\ln(K_1/B(T_S) + 1) \quad (3)$$

where  $K_1$  and  $K_2$  are calibration constants, which can be obtained from the metadata file. For Landsat 8,  $K_1 = 774.89 \text{ W}/(\text{m}^2 \cdot \mu\text{m} \cdot \text{sr})$  and  $K_2 = 1321.08 \text{ K}$ . For Landsat 9,  $K_1 = 799.03 \text{ W}/(\text{m}^2 \cdot \mu\text{m} \cdot \text{sr})$  and  $K_2 = 1329.24 \text{ K}$ .

To eliminate the systematic error resulting from different acquisition times of the two Landsat images for each season, we employed an image (path 122, row 44) as a reference and adjusted the retrieved LST of another image according to the invariant object method [55]. In addition, because the LST of an individual sampling point may be biased due to the ambient occlusion, we took the average value of the sampling

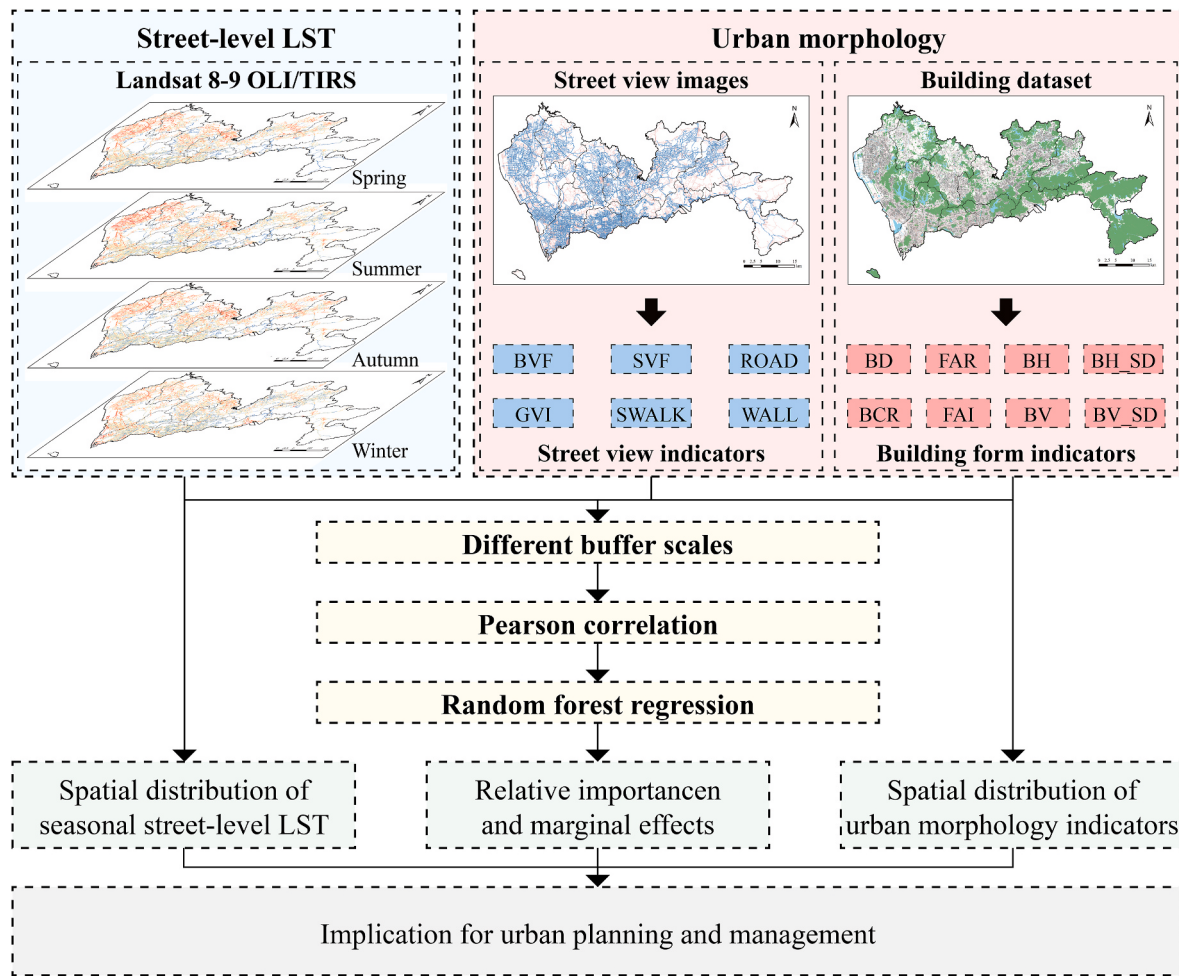


Fig. 2. Research framework.

points' LST within a buffer zone to reflect the urban thermal environment of streets.

### 3.2. Extraction of street view indicators

#### 3.2.1. Semantic image segmentation

Semantic segmentation is an important topic in computer vision (CV). It is able to identify elements in SVIs, allowing for the calculations of various indicators such as greenery quality, spatial openness and building enclosure [30]. Because the overexposure or underexposure of sky can happen due to the weather and time during photography, we found traditional Convolutional Neural Network (CNN) models like DeepLabV3+ did not perform well in recognizing sky area, whereas the Transformer models did better [56]. Thus, we used a transformer-based encoder-decoder model named SegFormer in this study. The coarse and fine features are extracted using a hierarchical Transformer encoder, and then the lightweight multilayer perceptron (MLP) decoder fuses these multi-level features to compute a semantic segmentation mask. Finally, the SVI whose each pixel is classified into given categories can be output [57]. The SegFormer architecture used in this study is shown in Fig. 3. After training with the Cityscapes dataset [58], the model could recognize 19 different classes with a mean Intersection over Union (mIoU) of 83.48%, the definition of 19 classes is shown in Appendix Table B.1. It also demonstrated good robustness in complex scenes with overexposure or underexposure.

#### 3.2.2. Conversion of fisheye images

The Street View Factors are important indicators describing the

urban street environment. The sky view factor (SVF) and the building view factor (BVF) are defined as the geometric ratios of the amount of visible sky and buildings respectively, from a given surface point to the overhead hemisphere of a transverse plane [59]. Calculating SVF and BVF needs to use fisheye images. The method of projecting panoramic SVIs from a cylindrical projection to an azimuthal projection to generate fisheye images had been shown to be reliable by in-situ measurement in previous study [36]. To further verify the reliability of the fisheye image conversion, we referred to the method proposed by Xia et al. [34]. A total of 100 fisheye images were randomly selected from the dataset. The sky pixels in fisheye images were manually extracted using Photoshop, and the proportion of sky pixels to total pixels was calculated. This ratio was then compared to the semantic segmentation outcomes with an  $R^2$  exceeding 0.98, which proved the reliability of the transformation. Fig. 4 shows the conversion process and Eqs. (4)–(8) show the calculation process.

In this case,  $W_p$  and  $H_p$  are the width and height of the panoramic image respectively. The radius of the fisheye image is  $r_0 = W_p/2\pi$ . Hence, the width and the height of the fisheye image are both  $W_p/\pi$ , and the center pixel  $(C_x, C_y)$  of the fisheye image is:

$$C_x = C_y = \frac{W}{2\pi} \quad (4)$$

For any pixel  $(x_f, y_f)$  on the fisheye image, its corresponding pixel on the panoramic image is  $(x_p, y_p)$ , as shown in Eqs. (5) and (6):

$$x_p = \frac{\theta}{2\pi} W_p \quad (5)$$

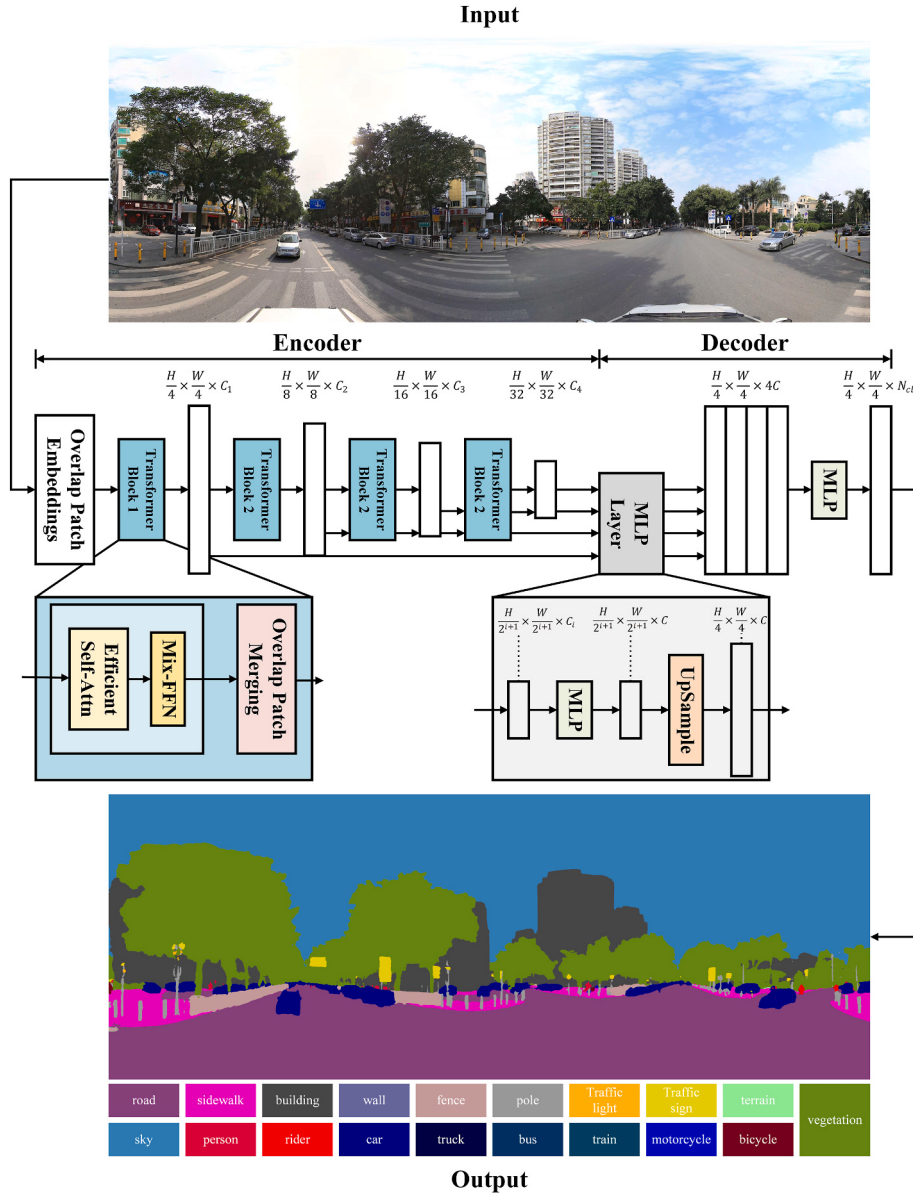


**Fig. 3.** The SegFormer framework.

$$y_p = \frac{r}{r_0} H_p \quad (6)$$

where  $\theta$  and  $r$  are given by:

$$\theta = \begin{cases} \frac{\pi}{2} + \tan^{-1} \left( \frac{y_f - C_y}{x_f - C_x} \right), & x_f < C_x \\ \frac{3\pi}{2} + \tan^{-1} \left( \frac{y_f - C_y}{x_f - C_x} \right), & x_f > C_x \end{cases} \quad (7)$$

$$r = \sqrt{(x_f - C_x)^2 + (y_f - C_y)^2} \quad (8)$$

All pixels are converted from the panoramic image to the fisheye image by using Eqs. (7) and (8). This process was implemented using Python 3.7 and OpenCV library.

### 3.2.3. Calculation of street view indicators

We obtained 19 categories after semantic segmentation. Considering the theoretical effect of each category on LST, we selected six indicators

as street view indicators used in subsequent analysis (Table 2). The GVI is calculated by the proportion of the greenery pixels in the panoramic image, which represents the visibility of environmental greening [50]. Calculating SVF and BVF requires extracting the sum of sky and building pixels in the fisheye image and calculating their proportions respectively [34,36]. The categories of road and sidewalk are considered as impervious surfaces, and the categories of building and wall are considered as artificial structures [60].

### 3.3. Calculation of building form indicators

In this study, eight building form indicators were proposed to investigate the seasonal effect mechanisms of LST, as shown in Table 3. BD indicates the intensity of land use and development [37,61]. FAR is used to evaluate land use efficiency [11,62]. BH and BH\_SD reflect the vertical construction intensity and the degree of height variation respectively [61,62]. BV measures the 3D morphology of buildings [63], and BV\_SD describes the diversity of building volumes [64]. Studies have shown that the building morphology at different heights within the urban canopy layer can alter airflow patterns [65]. Following the

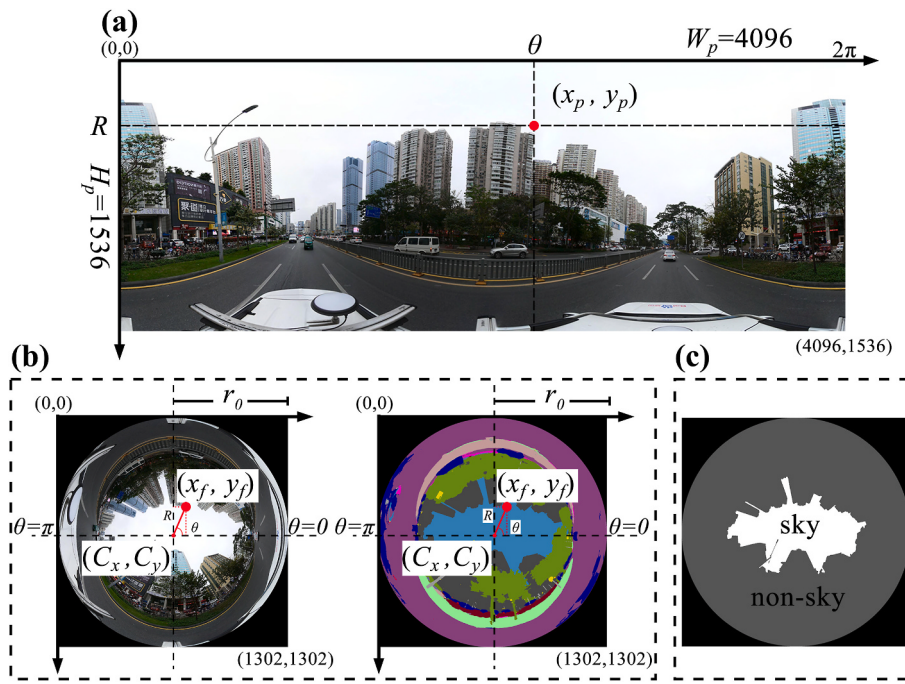


**Fig. 4.** The process of converting panoramic images to fisheye images: (a) Panoramic SVI; (b) Converting a panoramic image to a fisheye image; (c) Sky viewshed image.

**Table 2**  
Summary of street view indicators.

Street view indicators	Abbr.	Formula	Definition
Green view index	GVI	$GVI = \frac{Pixel_v + Pixel_t}{Pixel_p}$	$Pixel_v$ is the total number of pixels in vegetation, $Pixel_t$ is the total number of pixels in terrain, $Pixel_p$ is the total number of pixels in the panoramic image.
Percentage of wall	WALL	$WALL = \frac{Pixel_w}{Pixel_p}$	$Pixel_w$ is the total number of pixels in wall.
Percentage of road	ROAD	$ROAD = \frac{Pixel_r}{Pixel_p}$	$Pixel_r$ is the total number of pixels in road.
Percentage of sidewalk	SWALK	$SWALK = \frac{Pixel_{sw}}{Pixel_p}$	$Pixel_{sw}$ is the total number of pixels in sidewalk.
Sky view factor	SVF	$SVF = \frac{Pixel_s}{Pixel_f} \times \frac{4}{\pi}$	$Pixel_s$ is the total number of pixels in sky, and $Pixel_f$ is the total number of pixels in fisheye image.
Building view factor	BVF	$BVF = \frac{Pixel_b}{Pixel_f} \times \frac{4}{\pi}$	$Pixel_b$ is the total number of pixels in building.

method proposed by Xiong et al. [66], we firstly tested the Pearson correlations between BCR and LST for the BCR at various heights of 10 m, 20 m, 30 m, 40 m, 60 m, 80 m and 100 m. The BCR of 10 m which showed the highest correlation coefficient, was selected as the relevant indicator for this study. FAI describes the surface roughness of buildings so as to quantify the obstructions to wind flow within the urban canopy layer. Similar to BCR, we calculated the Pearson correlations between the FAIs in seven height intervals (0–10 m, 0–20 m, 0–30 m, 0–40 m, 0–60 m, 0–80 m and 0–100 m) and LST. The FAI of 0–10 m was finally selected as the indicator, whose correlation coefficient was the highest.

**Table 3**  
Summary of building form indicators.

Building form indicators	Abbr.	Formula	Definition
Building density	BD	$BD = \frac{\sum_{i=1}^n A_{bi}}{A_{buffer}}$	$A_{bi}$ is the base area of building $i$ , $n$ is the total number of buildings in the buffer zone, $A_{buffer}$ is the gross lot area of the buffer zone.
Floor area ratio	FAR	$FAR = \frac{\sum_{i=1}^n A_i}{A_{buffer}}$	$A_i$ is the total floor area of building $i$ .
Average building height	BH	$BH = \frac{\sum_{i=1}^n h_i}{n}$	$h_i$ is the height of building $i$ .
Standard deviation of building height	BH_SD	$BH\_SD = \sqrt{\frac{1}{n} \sum_{i=1}^n (h_i - \bar{h})^2}$	$\bar{h}$ is the average building height within the buffer zone.
Average building volume	BV	$BV = \frac{\sum_{i=1}^n V_i}{n}$	$V_i$ is the volume of building $i$ .
Standard deviation of building volume	BV_SD	$BV\_SD = \sqrt{\frac{1}{n} \sum_{i=1}^n (V_i - \bar{V})^2}$	$\bar{V}$ is the average building volume within the buffer zone.
Building coverage ratio	BCR	$BCR = \frac{\sum_{i=1}^n A_{bi,10}}{A_{buffer}}$	$A_{bi,10}$ is the area of building $i$ at 10 m.
Frontal area index	FAI	$FAI = \sum_{\theta=1}^{16} FAI_{(\theta)} P_{(\theta)}$	$FAI_{(\theta)}$ is the ratio of a projected windward building area $A_{proj}$ of 0–10 m to a unit horizontal area $A_T$ , expressed as $FAI_{(\theta)} = A_{proj}/A_T$ . $\theta$ is the wind direction measured in 16 different directions. $P_{(\theta)}$ is the annual average wind frequency in a particular direction.

### 3.4. Random forest regression

Firstly, the most appropriate buffer zone for the random forest (RF) regression was determined. Many studies have proved that the optimal influence radius of urban morphology is generally less than 250 m [16, 43, 61], and the area with radius  $\leq 250$  m roughly contains an urban block of Shenzhen. We implemented the Pearson correlations and RF regressions of urban morphology indicators and LSTs across four seasons, for five buffer zone radii ranging from 50 m to 250 m with an interval of 50 m. The results of Pearson correlations are presented in Appendix Table C.1 to Table C.5.

RF is a powerful machine learning technique that combines multiple decision trees to predict numerical values, which provides robustness against overfitting and enhances accuracy by averaging predictions from individual trees [23]. The relative importance and marginal effects of urban morphology indicators on street-level LST across the four seasons were investigated by the RF model. It was implemented using Python 3.7 and the scikit-learn machine learning library. During the modeling process, 75% of the data was randomly selected as the training dataset, and the remaining 25% was used as the testing dataset [16]. The overall coefficient of determination ( $R^2$ ) and the root mean square error (RMSE) of the testing dataset after 10-fold cross-validation were used to evaluate the model performance [39, 61]. To prevent overfitting and underfitting, a grid search algorithm named GridSearchCV function and the 5-fold cross-validation were used to identify the optimal parameters before model training [43]. Several parameters reported in previous studies which have the most significant impact on the model performance were adjusted: n\_estimators (the number of trees, ranging from 100 to 1000 with an interval of 100), max\_features (the number of features, ranging from 5 to 15 with an interval of 1) and max\_depth (the maximum depth, ranging from 1 to 15 with an interval of 1) [67, 68]. In hyper-parameter tuning process, the testing range of each parameter was initially set to be large to find the approximate range using coarse-grid search, and then the fine-tuning within the determined range was performed based on the  $R^2$  and RMSE from 5-fold cross-validation. The optimal values of them were summarized in Table 4, and other parameters were set as default values. The relative importance of each indicator was determined by the approach based on the Mean Decrease Impurity (MDI) named feature importance, which indicates the contribution of each indicator in LST variance [69]. To further interpret how each indicator affects LST, we used PDP to visualize whether the relationship between the indicator and LST is linear, monotonic, or more complex [70], as well as to investigate the maximum warming or cooling effect of each indicator [67]. We plotted PDPs for the indicators whose relative importance exceeded 5%.

## 4. Results

### 4.1. Optimal buffer zone scale

The results for different buffers across four seasons are shown in Table 5. The values in bold and underlined are the optimal results. It was shown that the  $R^2$  increases as the buffer radius increases for each season, and the most significant improvements were in the spring, summer, and autumn. The maximum  $R^2$  and the minimum RMSE were found at the 250 m buffer radius, which indicated it was the optimal scale for

**Table 4**  
The optimal parameters of RF models.

Season	Parameters		
	n_estimators	max_features	max_depth
Spring	700	9	15
Summer	800	9	15
Autumn	900	10	15
Winter	800	10	15

analyzing the relationship between urban morphology and street-level LST within the testing range. A larger buffer radius mitigates the adverse effects of extreme values of indicators and captures a wider range of building morphology beside roads, thereby improving the model's fitting performance. However, if the size continues to increase, it will possibly result in a significant change in the morphology of the building within the buffer zone (i.e., spanning multiple blocks), which may lead to a bias in the conclusions. Considering the accuracy and efficiency of analysis, this study used 250 m as the buffer radius.

### 4.2. Spatial distribution of LST and urban morphology indicators

The spatial distributions of LST in Shenzhen for four seasons are shown in Fig. 5. The ranges of LST were 16.39 °C-54.41 °C of Spring, 24.31 °C-64.86 °C of Summer, 20.06 °C-55.44 °C of Autumn and 10.56 °C-37.33 °C of Winter. The largest temperature difference in LST was observed during summer at 40.55 °C, and the smallest temperature difference occurred during winter at 26.77 °C. From these results, we found significant spatial heterogeneity in LST distribution. The heat islands were mainly located in the industrial areas of the western part of Bao'an District, Longhua District, Longgang District and Pingshan District, as well as in the areas covered by large artificial surface such as Bao'an Airport, Shenzhen Bay Port, Shekou Port and Yantian Port. Heat islands also occurred in densely populated and built-up areas. In contrast, cold islands were mainly distributed near mountains, large green parks and water bodies.

As shown in Fig. 6, the ranges of street-level LST for spring, summer, autumn and winter were 21.27 °C-41.74 °C, 25.98 °C-48.96 °C, 23.45 °C-43.46 °C and 11.39 °C-28.80 °C respectively. Similar to the results in Fig. 5, summer exhibited the largest temperature variation of 22.98 °C, while winter showed the smallest variation of 17.41 °C. Continuous hot streets were observed in the northwestern region of Baoan with the most severe condition occurring in summer. The northern intersection areas of Baoan and Guangming Districts as well as Longhua and Longgang Districts were also found continuous high-temperature regions. For the southern part of Bao'an District, Nanshan District, Futian District, Luohu District and the areas near airport and ports, there were only a limited number of continuous high-temperature roads within these regions. It is important to note that a large area with high-temperature roads was found near Yantian Port, and the roads in the built-up areas of Dapeng District exhibited high LST.

The spatial distribution of each street view indicators is shown in Fig. 7. The Green View Index (GVI) was significantly higher in the southern part of Bao'an District, Nanshan District, and Futian District compared to other areas. The WALL showed a relatively uniform distribution across the entire area, and with scattered high-value regions. The distributions of ROAD and SWALK presented opposite trends; higher ROAD values corresponded to lower SWALK values in the same area, for example. There was a significant correlation between ROAD and the urban road classification as well. The SVF exhibited high values in coastal areas, transportation hubs, and the regions with low building density, and it tended to be lower in the central area of each district. Specifically, continuous low-value SVF regions were found in the southern part of Bao'an District, Nanshan District, Bao'an District, and Luohu District. The spatial distribution of BVF was contrary to SVF, with higher values observed in central areas and lower values in coastal and low-density regions.

The spatial distribution of building form indicators is shown in Fig. 8. The BD exhibited the clustering of high values, reflecting compact building distribution. FAR illustrated a more distinct clustering of high values compared to BD. Continuous high-value distributions and high-value clusters were observed in the southern part of Bao'an District, Nanshan District, Futian District, Luohu District, Longhua District and Longgang District, which reflected the multi-center urban forms of Shenzhen. BH and BH\_SD reflected the vertical distribution and variations of buildings. In addition to high-value clusters in the central areas,

**Table 5**Comparisons of the  $R^2$  and RMSE of RF models for different buffer scales and seasons.

Buffer Scale (m)	$R^2$				RMSE			
	Spring	Summer	Autumn	Winter	Spring	Summer	Autumn	Winter
50	0.4769	0.4883	0.4388	0.2917	1.6388	1.9079	1.630	1.2488
100	0.5803	0.5812	0.5474	0.3794	1.4152	1.6859	1.4247	1.1096
150	0.6815	0.6375	0.6110	0.4456	1.2579	1.5004	1.2743	0.9958
200	0.7120	0.6973	0.6704	0.5148	1.0987	1.3481	1.1417	0.8840
250	<b>0.7956</b>	<b>0.7907</b>	<b>0.7642</b>	<b>0.6474</b>	<b>0.8976</b>	<b>1.0884</b>	<b>0.9256</b>	<b>0.7195</b>

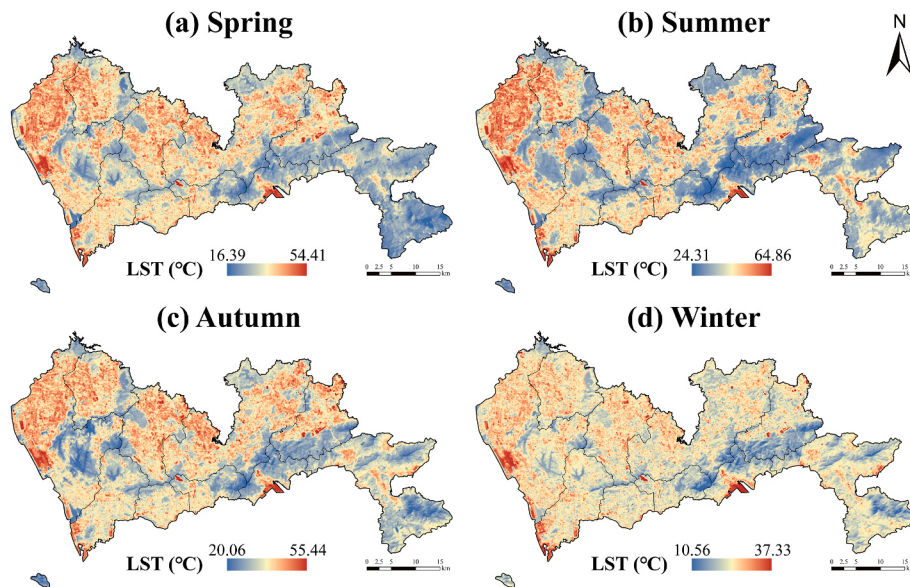


Fig. 5. The spatial distribution of seasonal LST in the study area.

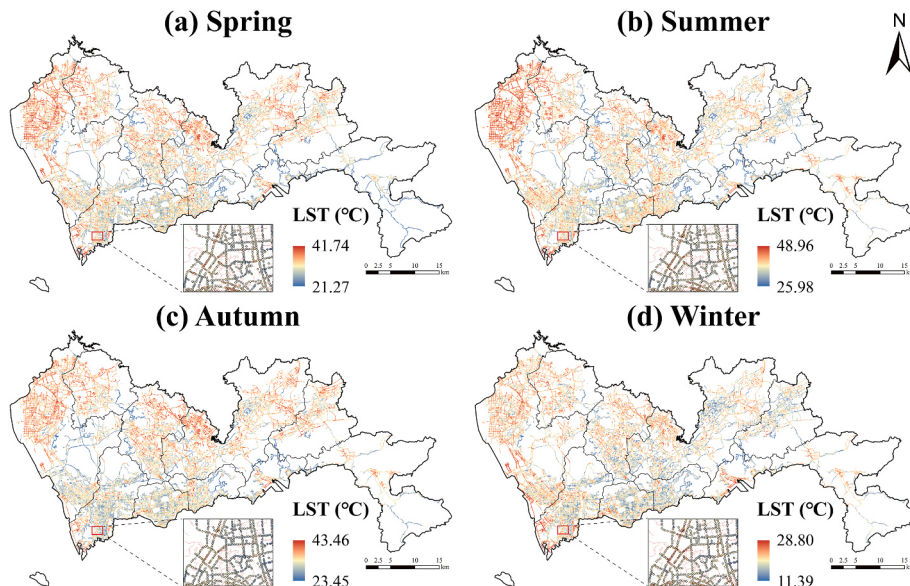
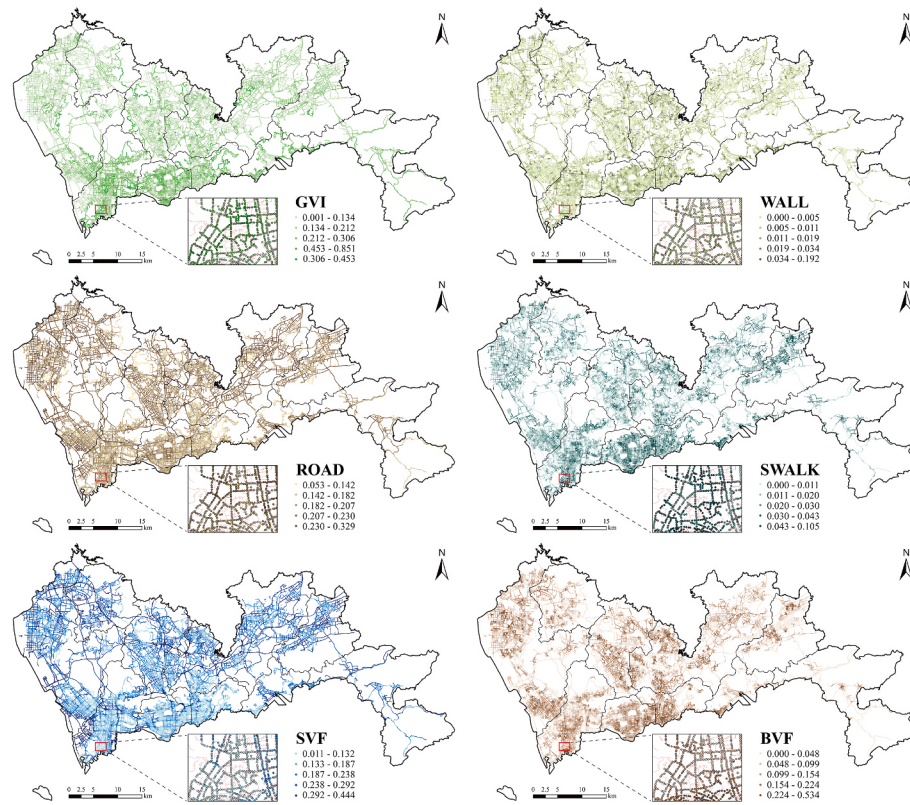


Fig. 6. The spatial distribution of seasonal street-level LST in the study area.

they also had localized high values. The high values of BV and BV\_SD exhibited scattered distributions and mainly occurred in Nanshan District and Futian District. The distribution patterns of BCR and FAI are similar to the distribution patterns of BD. Overall, the spatial distribution of building morphology in Shenzhen showed significant variations. Guangming District and the eastern Dapeng District had relatively lower

levels of development, whereas Bao'an District, Nanshan District, Futian District and Luohu District exhibited typical characteristics of high-density urban areas. Additionally, there were some areas with higher levels of development located at the junction areas between Longhua District and Longgang District, as well as in the eastern and central parts of Longgang District.



**Fig. 7.** The spatial distribution of street view indicators in the study area.

#### 4.3. The relative seasonal importance of urban morphology indicators

Fig. 9 depicts the seasonal relative importance of urban morphology indicators on street-level LST, in which building form indicators are in red and street view indicators are in blue. The  $R^2$  indicated that the RF models explained 79.56% of LST variations of spring, 79.07% of summer, 76.42% of autumn and 64.74% of winter. The total contribution of the six street view indicators dominated in all four seasons (spring: 67.59%, summer: 67.47%, autumn: 64.92%, winter: 60.61%). Specifically, BVF played key roles in spring and summer, and GVI was the most important indicator in autumn and winter. In spring, BVF explained 28.41% of LST variations while GVI, ROAD and SVF explained 19.77%, 6.53%, and 6.13% respectively. In summer, the most important indicator is BVF which contributed 28.88% to the explanation of LST variations whereas GVI, ROAD and SVF contributed 17.32%, 9.45% and 4.97% respectively. In autumn, the contribution of GVI (24.58%) surpassed that of BVF (19.70%), and ROAD and SVF contributed 7.80% and 5.07% respectively. In winter, the dominant indicators were the same as in autumn, with GVI and BVF contributing 17.73% and 13.41% respectively. The SVF (10.75%), ROAD (7.75%) and SWALK (6.10%) in winter have the highest contributions among the four seasons. Only the contribution of SWALK in winter was higher than 5%. The explanations of WALL were below 5% in all four seasons.

In terms of building form indicators, BD had the highest contributions in spring (11.14%) and summer (11.94%), while its contributions decreased in autumn (8.49%) and winter (4.98%). The explanations of BH and BH\_SD on LST variations showed significant variations across seasons. BH explained 4.65% in spring and 4.41% in summer; BH (10.31%) surpassed BD and became the most important building form indicator in winter. BH\_SD also showed higher relative importance in autumn (8.21%) and winter (6.62%) compared to spring (5.19%) and summer (2.68%). The contributions of FAR, BCR, BV, BV\_SD and FAI in each season were all below 5%, which indicated these indicators had relatively weak effects on LST. Considering the feasibility of urban

design and planning in mitigating the thermal environment of streets, we selected the indicators with relative importance greater than 5% to generate PDPs for further discussion.

#### 4.4. Seasonal marginal effects of urban morphology indicators

The Partial Dependence Plots (PDPs) in Fig. 10 display the nonlinear relationship between urban morphology indicators with relative importance greater than 5% and street-level LST for each season. The solid blue lines represent the average marginal effects, and the gray bars on the x-axis represent the distribution of the data. In cases where the data is sparsely distributed, the trend line of the marginal effects may not be accurate enough, and thus we will not discuss the results in such situations.

Results showed that each indicator exhibited similar patterns of marginal effects across different seasons, but had varying degrees of influence. For street view indicators, BVF ranged from 0.00 to 0.12 for four seasons. Within this range, an increase in the number of building pixels led to a rapid increase in LST, and the highest temperature increase ( $2.38^\circ\text{C}$ ) was observed in summer. Once the BVF exceeded 0.12, the LST tended to stabilize, indicating that the warming effect of BVF was limited to a certain range. Within the data distribution range of [0.00, 0.40], LST continuously decreased with the increase of GVI. The cooling effect of GVI in spring, summer, autumn, and winter was  $1.40^\circ\text{C}$ ,  $1.60^\circ\text{C}$ ,  $1.20^\circ\text{C}$  and  $0.90^\circ\text{C}$  respectively. Moreover, the cooling effect of GVI weakens when GVI exceeds 0.2 in winter. Within the interval [0.10, 0.30] for SVF, LST showed positive correlations with SVF, and the ranges of temperature rise were  $0.70^\circ\text{C}$  of spring,  $0.56^\circ\text{C}$  of summer,  $0.53^\circ\text{C}$  of autumn and  $0.60^\circ\text{C}$  of winter respectively. For the ROAD, LST initially showed positive correlations with ROAD and then exhibited varying degrees of negative correlations. The negative correlation was most significant in winter, with a turning point at around 0.20; the turning points were around 0.24 in other three seasons.

In terms of building form, BD showed positive correlations with LST,

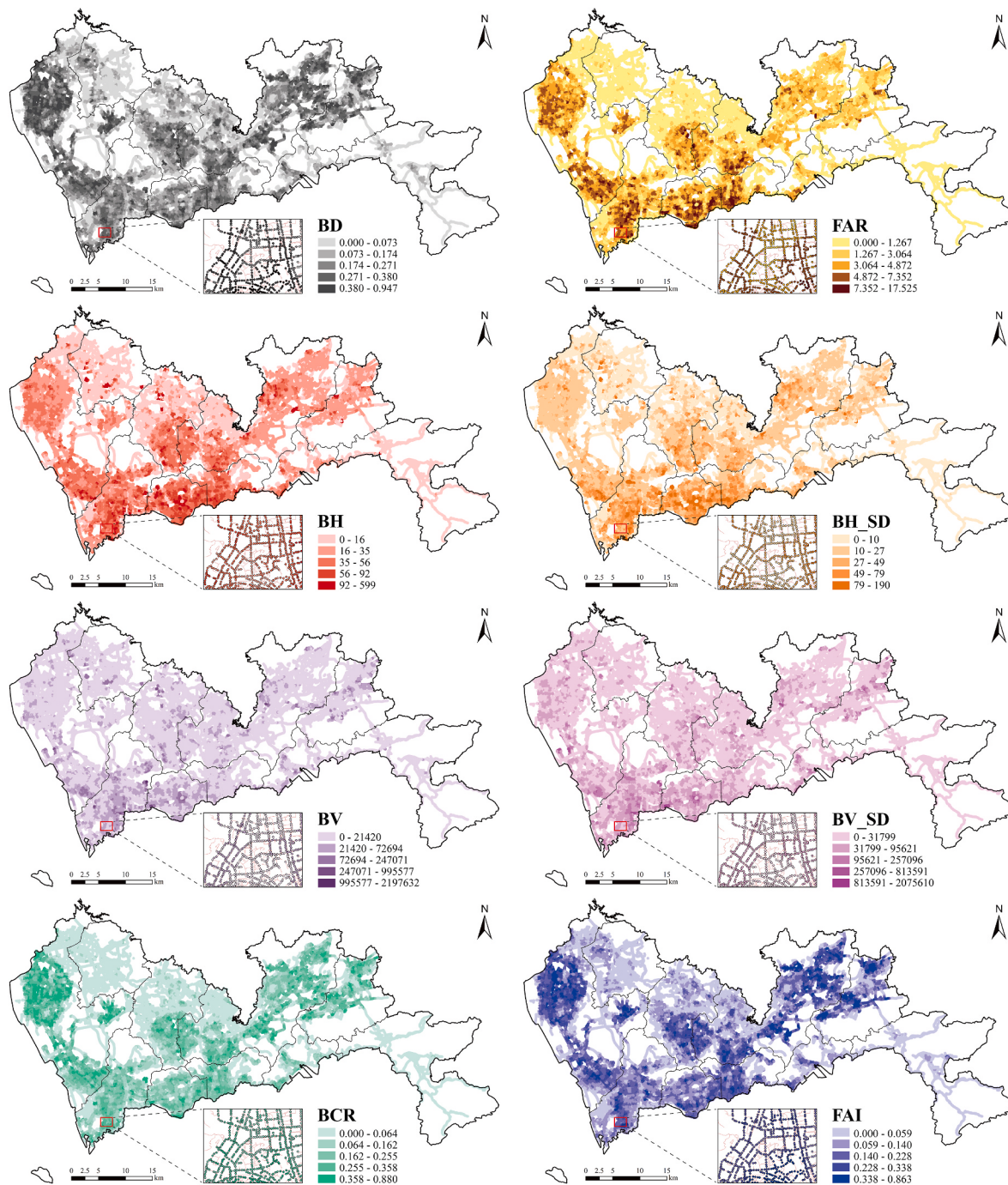


Fig. 8. The spatial distribution of building form indicators in the study area.

and the relations were approximately linear in spring, summer and autumn. The highest warming effect was observed in summer with an increase of 1.80 °C. In winter, the slope of the curve increased within the range of 0.32–0.40. For BH, there hardly was variation in LST across four seasons when BH ranged from 0 to 5 m. However, there were rapid decreases in LST once BH exceeded 5 m. The sensitivity of LST to BH also varied significantly across different seasons: the cooling effect of BH became weaker when BH reached 60 m, 20 m, 35 m and 90 m in spring, summer, autumn and winter respectively. The impact patterns of BH\_SD were more complex in the range of 0–15 m, where it exhibited intense fluctuations. When it was larger than 15 m, there were negative correlations between LST and BH\_SD, and the temperature drop of LST was 0.37 °C, 0.32 °C, 0.45 °C and 0.32 °C respectively for four seasons.

## 5. Discussion

### 5.1. Seasonal variations in the relative importance of urban morphology indicators

Although all indicators explained the variations of LST to some degree, there were differences in their relative importance across seasons. Similar to the findings of other studies [20], the dominant indicators in spring and summer were the same, and the dominant indicators in autumn and winter were also the same. In addition, the most important indicator in winter, GVI, whose contribution was lower than the dominant indicators in other seasons. This result suggests that the winter LST is influenced by the synergy of multiple indicators, but other seasons are

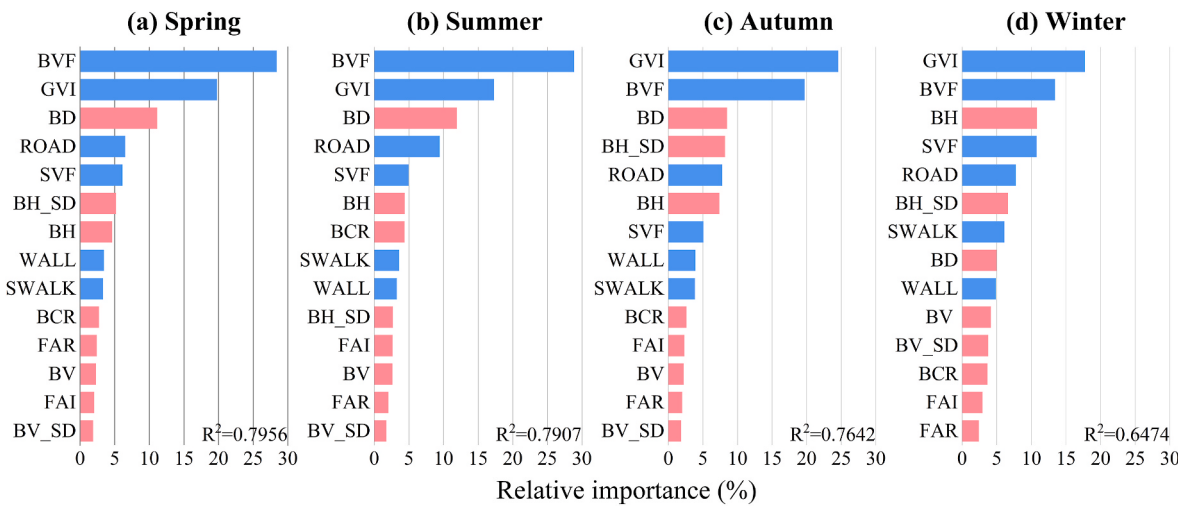


**Fig. 9.** The relative seasonal importance of urban morphology indicators on street-level LST.

influenced more by a single indicator. Similar conclusions have also been drawn for Wuhan and Hangzhou [16,42]. This result may be attributed to the significant reduction of daylight duration and intensity during winter in the Northern Hemisphere, leading to a decrease of solar radiation that may help to make the mechanisms that influence LST more complex [71]. The result of lower  $R^2$  of the RF model during winter compared to the other three seasons has also been reported in studies conducted in Beijing [41]. This result may be due to the smaller temperature variations of street-level LST during winter, making it more challenging for the model to capture subtle temperature differences. The study conducted by Berger et al. [63] in Berlin and Cologne also found a weaker association between urban building form and winter LST.

Compared with existing top-down remote sensing data sources, the predominant contributions of street view indicators indicate that the effects of street-level built environment elements on LST are also critical. In addition, street view indicators can precisely capture fine-grained information on built environment elements at street level, including vegetation, buildings and sky, which can help to better explain the variations in LST [72]. BVF and GVI consistently ranked among the top two of relative importance in all four seasons. A higher BVF value implies a higher planar and vertical construction intensity around the road. More buildings can lead to increased longwave radiation of urban canyons [36], and then exacerbate the thermal environment nearby. Various vegetation indicators have been shown to have an impact on LST [17,20,40]; this study also found that GVI had significant impacts on LST in all seasons and dominated the LST variations in autumn and winter. The cooling effect of plants is attributed to their ability to keep out direct sunlight, thereby reducing the radiation reached the ground and the process of transpiration from plants [17]. The categories of WALL, SWALK, and ROAD represented the common components of streets. The use of impermeable materials such as asphalt and concrete, which have low albedo and high solar radiation absorption rates, can contribute to the heating up of the street thermal environment [14]. Consisting with previous study [73], the contribution of ROAD in summer is the highest among the four seasons. Wider roads are likely to receive less shading, amplifying the impact of direct sunlight [74]. The relative importance of SVF in winter was significantly higher than that in other seasons, which differs from other studies. Li et al. [16] reported that SVF was significantly correlated with LST only in summer in Wuhan, and Hu et al. [38] found that SVF was important in both summer and winter in Beijing. This inconsistency may be caused by the differences in climate zones and urban morphology among different studies. Moreover, the grid-based statistical methods may average the LST and SVF within the buildings compared to our study conducted at the street-level.

BD, BH, and BH\_SD were important building form indicators that influenced LST, but their relative importance varied with the seasons. Similar to the study conducted in Nanjing [20], BD played a more important role in spring and summer, and its contribution decreased in autumn and winter; BH and BH\_SD exhibited increased importance in autumn and winter. According to a study conducted in Guangzhou [75], it was found that BD had a greater impact on LST compared to BH. However, our study found that BH had a higher relative importance than BD in winter. This difference could be caused by the lower solar altitude angle in winter which results in more shadow casting by buildings [16]. We also found the relatively weak impacts of FAR, BV, BV\_SD, BCR and FAI on LST. Previous studies have also shown that FAR had a relatively weak impact on LST [39–41]. This may be due to the fact that in areas with higher FAR, both BD and BH tend to be higher as well, thereby offsetting the impact. Berger et al. [63] reported a significant positive correlation between BV and LST, but the effect of BV was found to be very weak in our study. Xu et al. [62] demonstrated various importance of BV across different cities in their study, indicating that the influence of BV and BV\_SD may vary due to the differences of urban morphologies and climatic zones [19]. A study based on 62 different cities also demonstrated that the warming effect of BV on LST is mainly at night [76]. Additionally, the study conducted in Wuhan also confirmed that FAI had the least impact on LST among the five 3D urban morphology factors [16]. The fewer explanations of BCR and FAI in this study may be attributed to the fact that the FAI and BCR at 10 m height focus on describing the detailed composition of building forms. These two factors usually have a greater influence on local microclimate and wind environment within the block, which are more related to air temperature. By contrast, LST is more influenced by shortwave radiation and surface materials [16]. Moreover, different from the studies based on grids and administrative units, we focused on the effects of building morphology on street-level LST, whose results may differ from those within building blocks.

## 5.2. Seasonal marginal effects of urban morphology indicators

The PDP results demonstrated that the marginal effects of urban morphology indicators exhibited seasonal stability, which is consistent with previous studies [23,39,41]. In this study, BVF was found to cause an increase in LST, which is consistent with the research on building coverage [20,35,61]. A higher BVF indicates greater building coverage and enclosure, with building materials such as concrete having higher heat capacity and different surface radiative properties compared to vegetation. These materials absorb more solar radiation and emit longwave radiation through multiple reflections, leading to an increase

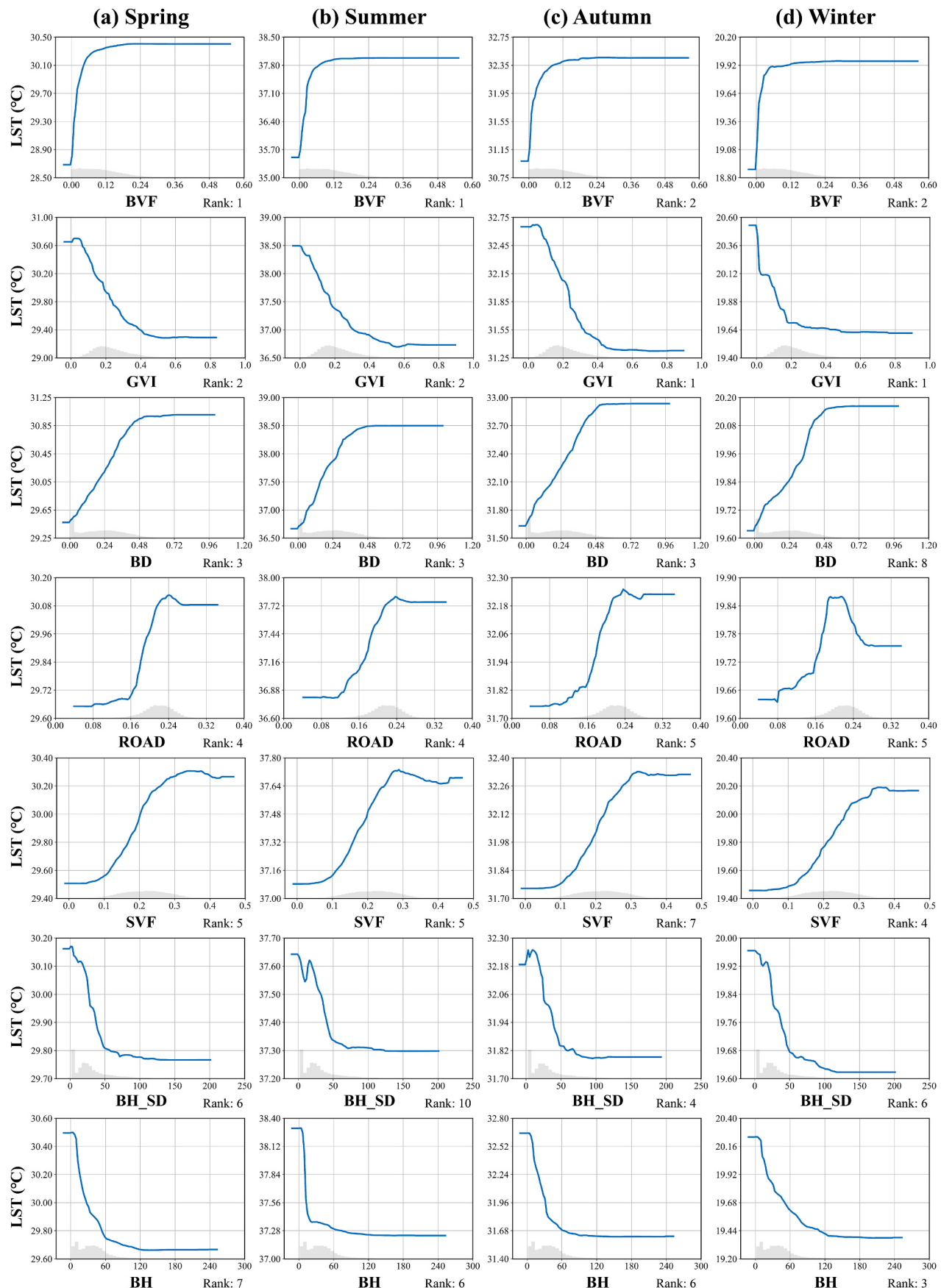


Fig. 10. The seasonal PDPs between urban morphology indicators and street-level LST.

in LST [2]. However, as BVF increased rapidly at first, the trends of LST became nearly steady. This result could be due to the fact that the building coverage in the horizontal direction has already reached a saturation point. Further increases in BVF imply the vertical growth of building pixels, which leads to increased shading from buildings, and this shading effect offsets the warming effect of longwave radiation from building surfaces on the ground. GVI provides a non-linear cooling effect, indicating that the presence of more visible vegetation in the street results in stronger cooling effect, which can significantly enhance the comfort of pedestrians and non-motorized vehicle users. The impacts of ROAD on LST varied across different seasons. As ROAD increased, LST initially rose rapidly but then decreased after reaching a value at around 0.20–0.24. The winter exhibited the most significant decrease, and the reason may be the cooling effect of enhanced air circulation surpasses the warming effect of solar radiation as the road width increased [23]. SVF affects LST through two aspects of ventilation and solar radiation. A higher SVF can enhance air convection so that reducing LST, but increased direct solar radiation can also lead to higher LST. Thus, the combined impact of SVF is determined by the trade-off between these two processes [16], and it is considered to be environment-dependent [11]. This study indicated that SVF had warming effects on LST in all seasons in Shenzhen, which may be due to the lower latitude of Shenzhen where the influence of solar radiation outweighs the effect of air circulation.

In terms of building form indicators, BD showed a similar warming pattern across all seasons, which is consistent with previous studies [16, 37, 41]. The increase in BD reduces green space and water area within the buffer zone, leading to an increase in LST through reducing heat storage capacity and evapotranspiration [11]. In winter, BD had a more significant impact on increasing LST. BH had cooling effects in all seasons consistent with previous research [16, 39, 61], but the cooling amplitude varies across seasons. Other studies have also reported the inflection points of BH effects, whereas they can differ due to research locations and scales [16, 18, 38]. It may be the result of the variations in building shadows caused by different latitudes and seasons [16]. Higher buildings provide shadows covering a larger area of impervious surfaces, such as building facades and roads, limiting the absorption of these surfaces to solar radiation [77]. High-rise buildings can even contribute to the urban cool island effect [78]. The negative correlation between BH\_SD has been showed in wind tunnel experiments. In street canyons, uneven building heights improve surface roughness, leading to mechanical turbulence and then enhancing convection heat dissipation [79]; uniform building heights can trap heat within compact structures and baffle ventilation.

### 5.3. Implications for urban planning and management

LST is related to the thermal comfort and health of residents. This study provided a scientific understanding of the seasonal impacts of urban morphology on street-level LST by analyzing and interpreting the relative importance and PDPs of RF models. The findings can provide valuable guidance for improving urban thermal environment. Based on our findings, BVF and GVI were the two most important indicators in four seasons, playing roles in warming and cooling respectively. Therefore, the coverage percentages of building and vegetation near streets should be given more attention since they determine the absorption and reflection of solar radiation on land surfaces. The “ForestaMi” project proposed by Milan aims to reduce 2 °C by planting three million new trees before 2030, and Melbourne has planned to increase urban forests and shadings for pedestrians to improve thermal comfort for residents [80]. However, it is necessary to consider the impact of urban greenery on available space for buildings. Some strategies may help minimize this trade-off. For instance, the application of green wall has great potential to mitigate the UHI effect in highly urbanized areas and reduce building energy consumption [81], which can reduce the BVF value while increasing the GVI in order to achieve a synergistic

cooling effect. In many countries, the city councils have implemented and subsidized the deployment of green wall to offset its high costs [81]. Green roof has been proved to be able to reduce the UHI effect regardless of climate zones [80]. Similarly, the implementation of green roof in a large area also requires a high capital cost [80]. Local governments are recommended to participate in the decision-making and provide financial support for the large-scale promotion. The arrangement of different vegetation types can also affect the cooling effect [67]. The use of trees in hot areas is more beneficial than that of grass as they provide shade to reduce building and road temperatures. Considering the mild winter climate in Shenzhen, the use of evergreen vegetation can also provide good cooling effects during winter [38]. Building parks and water bodies within the city can also contribute beneficially to controlling LST [40]. It is also suggested to utilize high albedo pavement materials, water-retentive materials and heat-capturing devices for roads and sidewalks [82]. A study conducted in Paris demonstrated that regularly watering road surfaces can increase albedo and reduce thermal stress [83], which is also one of the cooling strategies currently being implemented in Shenzhen. Additionally, on the premise of ensuring the daylighting of buildings and roadways, lower SVF is conducive to reducing the street-level LST in Shenzhen. Therefore, in future urban planning and design, the element composition and ratio of streetscape also need comprehensive assessment.

We found that the building forms within a radius of 250 m from the sampling points on the road have a significant impact on LST, which is a typical planning unit of urban block in Shenzhen [84]. The mitigation strategies for UHI focusing on building layout and spatial form are suggested to be implemented within this scale. Considering the interactions among BD, BH and BH\_SD, new-built communities are recommended to prioritize low-density and high-rise buildings, as well as avoid uniform building heights [41]. In addition, Shenzhen has numerous self-built urban villages in the inner-city area, the morphology of which (high-density, low-rise and low-standard deviation building blocks) remained a distinct feature of urban landscape. During the urban renewal of urban villages, certain buildings can be demolished and high-rise low-density building blocks are recommended to mitigate the warming effect of these dense blocks. Although FAR, BV, BV\_SD, BCR, and FAI had relatively small impacts on LST, these indicators are still associated with urban ventilation, sunlight exposure and energy consumption, which should also be considered during urban planning and design. Currently, new construction projects in Shenzhen require a comprehensive assessment report on the impact of the physical environment nearby, including outdoor thermal environment. The projects that significantly worsen surrounding thermal environment cannot be approved, which is a good start to ensure environmental sustainability. Given the long coastline of Shenzhen, the impact of wind on the heat balance of the city cannot be ignored. Ventilation corridors are encouraged to be planned to help remove excessive heat. Additionally, although our conclusions are based on a case study, the methodology can also be applied to the research in other cities. Finally, improving urban thermal environment is a huge and intricate task that requires a comprehensive consideration of the aforementioned strategies and the collaborations of governments, utilities and all residents.

### 5.4. Limitations and future research

This study still has some limitations. First, it focused on the influence of building form and street view on street-level LST in Shenzhen during a specific time of day captured by Landsat 8–9 satellites between 10:45–10:52 a.m. However, time and climate are also important factors affecting LST [19, 23]. Future research could utilize MODIS satellite products to obtain daytime and nighttime LST data, and validate our findings across cities in multiple climatic zones. Second, although the spatial resolution of Landsat 8–9 reaches 30 m, it is still insufficient for the research scale of urban streets and buildings. The use of unmanned aerial vehicles (UAVs) equipped with thermal infrared sensors can be

employed to acquire higher-precision LST as well as building and vegetation models. Third, semantic segmentation can classify vegetation types more precisely, such as trees, shrubs and grass, which can be used to investigate their importance and patterns of influence on LST even further. Moreover, the indicators that influence the urban thermal environment are complicated. It is recommended to incorporate multi-source data based on big data analysis in the future, e.g., traffic volume, distributions of Points of Interest (POI) and distances to different land-use areas [17,35,67]. Finally, the comparison of different Machine Learning models may also lead to some new insights [22,45], we will implement in the future.

## 6. Conclusion

This study investigated the effects of building form and street view indicators on street-level LST. We employed SVI, 3D building dataset and remote sensing satellite imagery as multi-source data, and proposed 14 urban morphology indicators including building form and street view parameters. The RF models were applied to determine the interaction mechanisms between urban morphology and LST across four seasons by means of relative importance and marginal effects. The results confirm that urban morphology is a crucial aspect influencing street-level LST. The established RF models explained 79.56%, 79.07%, 76.42% and 64.74% of the LST variations in spring, summer, autumn and winter respectively. Among all indicators we proposed, the street view indicators were proved to have a main impact on LST compared to the building form indicators. The total contribution of street view indicators in each season exceeded 60%. We also found main influencing factors for each season. BVF was the dominant indicator for LST in spring and summer, followed by GVI and BD. The dominant factors were GVI and BVF for autumn and winter. The highest contribution of SVF was found in winter. BD had higher relative importance in spring and summer compared to autumn and winter, while the importance of BH and BH\_SD significantly increased in autumn and winter. The contributions of BV, BV\_SD, FAR, BCR and FAI to LST variations were all below 5% in each season. The nonlinear relationships between key urban morphology and LST were also determined. The marginal effects of urban morphology indicators on LST exhibited good stability across four seasons except for ROAD. BVF, BD and SVF showed varying degrees of warming effects in all seasons with BVF exhibiting the highest warming effect of up to 2.38 °C in summer. GVI, BH, and BH\_SD demonstrated cooling effects in all seasons with GVI exhibiting the highest cooling effect of up to 1.60 °C in summer. This study provides evidence of the crucial indicators that influence street-level LST and the underlying mechanisms, which can assist urban planners and policymakers to better understand the formation of the UHI effect and implement mitigation strategies. By utilizing the findings of this research, planners can create more sustainable and livable cities that can better address the challenges from rising temperatures and extreme weather events.

## CRediT authorship contribution statement

**Keyan Chen:** Writing – review & editing, Writing – original draft, Visualization, Software, Methodology, Data curation, Conceptualization. **Meng Tian:** Writing – review & editing, Supervision, Project administration, Methodology, Formal analysis. **Jianfeng Zhang:** Validation, Software, Methodology. **Xuesong Xu:** Supervision, Project administration, Funding acquisition. **Lei Yuan:** Resources, Project administration, Investigation, Funding acquisition.

## Declaration of competing interest

The authors declare that they have no known competing financial interests or personal relationships that could have appeared to influence the work reported in this paper.

## Data availability

Data will be made available on request.

## Acknowledgment

This study was supported by the Guangdong Science and Technology Department (2023A1515011647) and the Science, Technology and Innovation Commission of Shenzhen Municipality (JCYJ20180305125219726).

## Appendix A. Supplementary data

Supplementary data to this article can be found online at <https://doi.org/10.1016/j.buildenv.2023.110884>.

## References

- [1] N.B. Grimm, S.H. Faeth, N.E. Golubiewski, C.L. Redman, J. Wu, X. Bai, J.M. Briggs, Global change and the ecology of cities, *Science* 319 (2008) 756–760, <https://doi.org/10.1126/science.1150195>.
- [2] T.R. Oke, The energetic basis of the urban heat island, *Q. J. R. Meteorol. Soc.* 108 (1982) 1–24, <https://doi.org/10.1002/qj.49710845502>.
- [3] M. Palme, L. Inostroza, G. Villacreses, A. Lobato-Cordero, C. Carrasco, From urban climate to energy consumption. Enhancing building performance simulation by including the urban heat island effect, *Energy Build.* 145 (2017) 107–120, <https://doi.org/10.1016/j.enbuild.2017.03.069>.
- [4] S. Guhathakurta, P. Gober, The impact of the Phoenix urban heat island on residential water use, *J. Am. Plann. Assoc.* 73 (2007) 317–329, <https://doi.org/10.1080/01944360708977980>.
- [5] J. Ngarambe, S.J. Joen, C.-H. Han, G.Y. Yun, Exploring the relationship between particulate matter, CO, SO<sub>2</sub>, NO<sub>2</sub>, O<sub>3</sub> and urban heat island in Seoul, Korea, *J. Hazard Mater.* 403 (2021), 123615, <https://doi.org/10.1016/j.jhazmat.2020.123615>.
- [6] F. Salata, I. Golasi, D. Petitti, E. de Lieto Vollaro, M. Coppi, A. de Lieto Vollaro, Relating microclimate, human thermal comfort and health during heat waves: an analysis of heat island mitigation strategies through a case study in an urban outdoor environment, *Sustain. Cities Soc.* 30 (2017) 79–96, <https://doi.org/10.1016/j.scs.2017.01.006>.
- [7] B.-J. He, L. Ding, D. Prasad, Urban ventilation and its potential for local warming mitigation: a field experiment in an open low-rise gridiron precinct, *Sustain. Cities Soc.* 55 (2020), 102028, <https://doi.org/10.1016/j.scs.2020.102028>.
- [8] J. Song, H. Yu, Y. Lu, Spatial-scale dependent risk factors of heat-related mortality: a multiscale geographically weighted regression analysis, *Sustain. Cities Soc.* 74 (2021), 103159, <https://doi.org/10.1016/j.scs.2021.103159>.
- [9] C. Tuholiske, K. Taylor, C. Funk, A. Verdin, S. Sweeney, K. Grace, P. Peterson, T. Evans, Global urban population exposure to extreme heat, *Proc. Natl. Acad. Sci. U.S.A.* 118 (2021), e2024792118, <https://doi.org/10.1073/pnas.2024792118>.
- [10] F. Binarti, P. Pranowo, S.B. Leksono, Thermal infrared images to identify the contribution of surface materials to the canopy layer heat island in hot-humid urban areas, *Environ. Clim. Technol.* 24 (2020) 604–623, <https://doi.org/10.2478/rteuct-2020-0037>.
- [11] X. Huang, Y. Wang, Investigating the effects of 3D urban morphology on the surface urban heat island effect in urban functional zones by using high-resolution remote sensing data: a case study of Wuhan, Central China, *ISPRS J. Photogrammetry Remote Sens.* 152 (2019) 119–131, <https://doi.org/10.1016/j.isprsjprs.2019.04.010>.
- [12] F. Yuan, M.E. Bauer, Comparison of impervious surface area and normalized difference vegetation index as indicators of surface urban heat island effects in Landsat imagery, *Rem. Sens. Environ.* 106 (2007) 375–386, <https://doi.org/10.1016/j.rse.2006.09.003>.
- [13] D. Zhou, S. Zhao, S. Liu, L. Zhang, C. Zhu, Surface urban heat island in China's 32 major cities: spatial patterns and drivers, *Rem. Sens. Environ.* 152 (2014) 51–61, <https://doi.org/10.1016/j.rse.2014.05.017>.
- [14] C. Yin, M. Yuan, Y. Lu, Y. Huang, Y. Liu, Effects of urban form on the urban heat island effect based on spatial regression model, *Sci. Total Environ.* 634 (2018) 696–704, <https://doi.org/10.1016/j.scitotenv.2018.03.350>.
- [15] H. Farhadi, M. Faizi, H. Sanaieian, Mitigating the urban heat island in a residential area in Tehran: investigating the role of vegetation, materials, and orientation of buildings, *Sustain. Cities Soc.* 46 (2019), 101448, <https://doi.org/10.1016/j.scs.2019.101448>.
- [16] H. Li, Y. Li, T. Wang, Z. Wang, M. Gao, H. Shen, Quantifying 3D building form effects on urban land surface temperature and modeling seasonal correlation patterns, *Build. Environ.* 204 (2021), 108132, <https://doi.org/10.1016/j.buildenv.2021.108132>.
- [17] Q. Wang, X. Wang, Y. Zhou, D. Liu, H. Wang, The dominant factors and influence of urban characteristics on land surface temperature using random forest algorithm, *Sustain. Cities Soc.* 79 (2022), 103722, <https://doi.org/10.1016/j.scs.2022.103722>.

- [18] A. Guo, W. Yue, J. Yang, T. He, M. Zhang, M. Li, Divergent impact of urban 2D/3D morphology on thermal environment along urban gradients, *Urban Clim.* 45 (2022), 101278, <https://doi.org/10.1016/j.ulclim.2022.101278>.
- [19] S. Cao, Y. Cai, M. Du, Q. Weng, L. Lu, Seasonal and diurnal surface urban heat islands in China: an investigation of driving factors with three-dimensional urban morphological parameters, *GIScience Remote Sens.* 59 (2022) 1121–1142, <https://doi.org/10.1080/15481603.2022.2100100>.
- [20] J. Chen, W. Zhan, P. Du, L. Li, J. Li, Z. Liu, F. Huang, J. Lai, J. Xia, Seasonally disparate responses of surface thermal environment to 2D/3D urban morphology, *Build. Environ.* 214 (2022), 108928, <https://doi.org/10.1016/j.buildenv.2022.108928>.
- [21] C.S.B. Grimmond, T.R. Oke, Aerodynamic properties of urban areas derived from analysis of surface form, *J. Appl. Meteorol.* 38 (1999) 1262–1292, [https://doi.org/10.1175/1520-0450\(1999\)038<1262:APOUAD>2.0.CO;2](https://doi.org/10.1175/1520-0450(1999)038<1262:APOUAD>2.0.CO;2).
- [22] T.M. Logan, B. Zaitchik, S. Guikema, A. Nisbet, Night and day: the influence and relative importance of urban characteristics on remotely sensed land surface temperature, *Rem. Sens. Environ.* 247 (2020), 111861, <https://doi.org/10.1016/j.rse.2020.111861>.
- [23] F. Guo, Q. Wu, U. Schlink, 3D building configuration as the driver of diurnal and nocturnal land surface temperatures: application in Beijing's old city, *Build. Environ.* 206 (2021), 108354, <https://doi.org/10.1016/j.buildenv.2021.108354>.
- [24] L. Yang, K. Yu, J. Ai, Y. Liu, W. Yang, J. Liu, Dominant factors and spatial heterogeneity of land surface temperatures in urban areas: a case study in Fuzhou, China, *Rem. Sens.* 14 (2022) 1266, <https://doi.org/10.3390/rs14051266>.
- [25] Y. Gao, J. Zhao, L. Han, Exploring the spatial heterogeneity of urban heat island effect and its relationship to block morphology with the geographically weighted regression model, *Sustain. Cities Soc.* 76 (2022), 103431, <https://doi.org/10.1016/j.scs.2021.103431>.
- [26] M. Deng, W. Yang, C. Chen, Z. Wu, Y. Liu, C. Xiang, Street-level solar radiation mapping and patterns profiling using Baidu Street View images, *Sustain. Cities Soc.* 75 (2021), 103289, <https://doi.org/10.1016/j.scs.2021.103289>.
- [27] K. Paunović, B. Jakovljević, G. Belojević, Predictors of noise annoyance in noisy and quiet urban streets, *Sci. Total Environ.* 407 (2009) 3707–3711, <https://doi.org/10.1016/j.scitotenv.2009.02.033>.
- [28] C. Wu, Y. Ye, F. Gao, X. Ye, Using street view images to examine the association between human perceptions of locale and urban vitality in Shenzhen, China, *Sustain. Cities Soc.* 88 (2023), 104291, <https://doi.org/10.1016/j.scs.2022.104291>.
- [29] Y. Zhang, A. Middel, B.L. Turner, Evaluating the effect of 3D urban form on neighborhood land surface temperature using Google Street View and geographically weighted regression, *Landsat. Ecol.* 34 (2019) 681–697, <https://doi.org/10.1007/s10980-019-00794-y>.
- [30] Y. Xia, N. Yabuki, T. Fukuda, Development of a system for assessing the quality of urban street-level greenery using street view images and deep learning, *Urban For. Urban Green.* 59 (2021), 126995, <https://doi.org/10.1016/j.ufug.2021.126995>.
- [31] F. Biljecki, K. Ito, Street view imagery in urban analytics and GIS: a review, *Landsat. Urban Plann.* 215 (2021), 104217, <https://doi.org/10.1016/j.landurbplan.2021.104217>.
- [32] Y. Kumakoshi, S.Y. Chan, H. Koizumi, X. Li, Y. Yoshimura, Standardized green view index and quantification of different metrics of urban green vegetation, *Sustainability* 12 (2020) 7434, <https://doi.org/10.3390/su12187434>.
- [33] K. Du, J. Ning, L. Yan, How long is the sun duration in a street canyon? — analysis of the view factors of street canyons, *Build. Environ.* 172 (2020), 106680, <https://doi.org/10.1016/j.buildenv.2020.106680>.
- [34] Y. Xia, N. Yabuki, T. Fukuda, Sky view factor estimation from street view images based on semantic segmentation, *Urban Clim.* 40 (2021), 100999, <https://doi.org/10.1016/j.ulclim.2021.100999>.
- [35] Q. Wang, X. Wang, Y. Meng, Y. Zhou, H. Wang, Exploring the impact of urban features on the spatial variation of land surface temperature within the diurnal cycle, *Sustain. Cities Soc.* 91 (2023), 104432, <https://doi.org/10.1016/j.scs.2023.104432>.
- [36] F.-Y. Gong, Z.-C. Zeng, F. Zhang, X. Li, E. Ng, L.K. Norford, Mapping sky, tree, and building view factors of street canyons in a high-density urban environment, *Build. Environ.* 134 (2018) 155–167, <https://doi.org/10.1016/j.buildenv.2018.02.042>.
- [37] X. Liu, Y. Ming, Y. Liu, W. Yue, G. Han, Influences of landform and urban form factors on urban heat island: comparative case study between Chengdu and Chongqing, *Sci. Total Environ.* 820 (2022), 153395, <https://doi.org/10.1016/j.scitotenv.2022.153395>.
- [38] Y. Hu, Z. Dai, J.-M. Guldmann, Modeling the impact of 2D/3D urban indicators on the urban heat island over different seasons: a boosted regression tree approach, *J. Environ. Manag.* 266 (2020), 110424, <https://doi.org/10.1016/j.jenvman.2020.110424>.
- [39] F. Sun, M. Liu, Y. Wang, H. Wang, Y. Che, The effects of 3D architectural patterns on the urban surface temperature at a neighborhood scale: relative contributions and marginal effects, *J. Clean. Prod.* 258 (2020), 120706, <https://doi.org/10.1016/j.jclepro.2020.120706>.
- [40] B. Yuan, L. Zhou, X. Dang, D. Sun, F. Hu, H. Mu, Separate and combined effects of 3D building features and urban green space on land surface temperature, *J. Environ. Manag.* 295 (2021), 113116, <https://doi.org/10.1016/j.jenvman.2021.113116>.
- [41] D. Han, H. An, F. Wang, X. Xu, Z. Qiao, M. Wang, X. Sui, S. Liang, X. Hou, H. Cai, Y. Liu, Understanding seasonal contributions of urban morphology to thermal environment based on boosted regression tree approach, *Build. Environ.* 226 (2022), 109770, <https://doi.org/10.1016/j.buildenv.2022.109770>.
- [42] S. Han, H. Hou, R.C. Estoque, Y. Zheng, C. Shen, Y. Murayama, J. Pan, B. Wang, T. Hu, Seasonal effects of urban morphology on land surface temperature in a three-dimensional perspective: a case study in Hangzhou, China, *Build. Environ.* vol. 228 (2023), 109913, <https://doi.org/10.1016/j.buildenv.2022.109913>.
- [43] Y. Chen, J. Yang, W. Yu, J. Ren, X. Xiao, J.C. Xia, Relationship between urban spatial form and seasonal land surface temperature under different grid scales, *Sustain. Cities Soc.* 89 (2023), 104374, <https://doi.org/10.1016/j.scs.2022.104374>.
- [44] M. Belgiu, L. Drăguț, Random forest in remote sensing: a review of applications and future directions, *ISPRS J. Photogrammetry Remote Sens.* 114 (2016) 24–31, <https://doi.org/10.1016/j.isprsjprs.2016.01.011>.
- [45] X. Ren, Z. Mi, P.G. Georgopoulos, Comparison of Machine Learning and Land Use Regression for fine scale spatiotemporal estimation of ambient air pollution: modeling ozone concentrations across the contiguous United States, *Environ. Int.* 142 (2020), 105827, <https://doi.org/10.1016/j.envint.2020.105827>.
- [46] Y. Ye, D. Li, X. Liu, How block density and typology affect urban vitality: an exploratory study in Shenzhen, China, *Urban Geogr.* 39 (2018) 631–652, <https://doi.org/10.1080/02723638.2017.1381536>.
- [47] J. Peng, J. Jia, Y. Liu, H. Li, J. Wu, Seasonal contrast of the dominant factors for spatial distribution of land surface temperature in urban areas, *Rem. Sens. Environ.* 215 (2018) 255–267, <https://doi.org/10.1016/j.rse.2018.06.010>.
- [48] W. Yu, C. Jing, W. Zhou, W. Wang, Z. Zheng, Time-series Landsat data for 3D reconstruction of urban history, *Rem. Sens.* 13 (2021) 4339, <https://doi.org/10.3390/rs131214339>.
- [49] D. Ki, S. Lee, Analyzing the effects of Green View Index of neighborhood streets on walking time using Google Street View and deep learning, *Landsat. Urban Plann.* 205 (2021), 103920, <https://doi.org/10.1016/j.landurbplan.2020.103920>.
- [50] J. Hua, M. Cai, Y. Shi, C. Ren, J. Xie, L.C.H. Chung, Y. Lu, L. Chen, Z. Yu, C. Webster, Investigating pedestrian-level greenery in urban forms in a high-density city for urban planning, *Sustain. Cities Soc.* 80 (2022), 103755, <https://doi.org/10.1016/j.scs.2022.103755>.
- [51] R. Wang, Z. Feng, J. Pearce, Y. Yao, X. Li, Y. Liu, The distribution of greenspace quantity and quality and their association with neighbourhood socioeconomic conditions in Guangzhou, China: a new approach using deep learning method and street view images, *Sustain. Cities Soc.* 66 (2021), 102664, <https://doi.org/10.1016/j.scs.2020.102664>.
- [52] X. Yu, X. Guo, Z. Wu, Land surface temperature retrieval from Landsat 8 TIRS—comparison between radiative transfer equation-based method, split window algorithm and single channel method, *Rem. Sens.* 6 (2014) 9829–9852, <https://doi.org/10.3390/rs6109829>.
- [53] J.C. Jimenez-Munoz, J.A. Sobrino, D. Skokovic, C. Mattar, J. Cristobal, Land surface temperature retrieval methods from Landsat-8 thermal infrared sensor data, *IEEE Geosci. Rem. Sens. Lett.* 11 (2014) 1840–1843, <https://doi.org/10.1109/LGRS.2014.2312032>.
- [54] Z. Yu, X. Guo, G. Jørgensen, H. Vejre, How can urban green spaces be planned for climate adaptation in subtropical cities? *Ecol. Indicat.* 82 (2017) 152–162, <https://doi.org/10.1016/j.ecolind.2017.07.002>.
- [55] W. Li, Q. Cao, K. Lang, J. Wu, Linking potential heat source and sink to urban heat island: heterogeneous effects of landscape pattern on land surface temperature, *Sci. Total Environ.* 586 (2017) 457–465, <https://doi.org/10.1016/j.scitotenv.2017.01.191>.
- [56] A. Dosovitskiy, L. Beyer, A. Kolesnikov, D. Weissenborn, X. Zhai, T. Unterthiner, M. Dehghani, M. Minderer, G. Heigold, S. Gelly, J. Uszkoreit, N. Houlsby, An Image Is Worth 16x16 Words: Transformers for Image Recognition at Scale, 2021, 11929, <http://arxiv.org/abs/2010.11929>. (Accessed 13 March 2023).
- [57] E. Xie, W. Wang, Z. Yu, A. Anandkumar, J.M. Alvarez, P. Luo, SegFormer: Simple and Efficient Design for Semantic Segmentation with Transformers, 2021, <http://arxiv.org/abs/2105.15203>. (Accessed 23 December 2022).
- [58] M. Cordts, M. Omran, S. Ramos, T. Rehfeld, M. Enzweiler, R. Benenson, U. Franke, S. Roth, B. Schiele, The Cityscapes Dataset for Semantic Urban Scene Understanding, 2016, <http://arxiv.org/abs/1604.01685>. (Accessed 8 October 2022).
- [59] G.T. Johnson, I.D. Watson, The determination of view-factors in urban canyons, *J. Clim. Appl. Meteorol.* 23 (1984) 329–335, [https://doi.org/10.1175/1520-0450\(1984\)023<0329:TDOVFI>2.0.CO;2](https://doi.org/10.1175/1520-0450(1984)023<0329:TDOVFI>2.0.CO;2).
- [60] A. Middel, J. Lukasczyk, S. Zakrzewski, M. Arnold, R. Maciejewski, Urban form and composition of street canyons: a human-centric big data and deep learning approach, *Landsat. Urban Plann.* 183 (2019) 122–132, <https://doi.org/10.1016/j.landurbplan.2018.12.001>.
- [61] Z. Li, D. Hu, Exploring the relationship between the 2D/3D architectural morphology and urban land surface temperature based on a boosted regression tree: a case study of Beijing, China, *Sustain. Cities Soc.* 78 (2022), 103392, <https://doi.org/10.1016/j.scs.2021.103392>.
- [62] H. Xu, C. Li, Y. Hu, S. Li, R. Kong, Z. Zhang, Quantifying the effects of 2D/3D urban landscape patterns on land surface temperature: a perspective from cities of different sizes, *Build. Environ.* 233 (2023), 110085, <https://doi.org/10.1016/j.buildenv.2023.110085>.
- [63] C. Berger, J. Rosentreter, M. Voltersen, C. Baumgart, C. Schmullius, S. Hese, Spatio-temporal analysis of the relationship between 2D/3D urban site characteristics and land surface temperature, *Rem. Sens. Environ.* 193 (2017) 225–243, <https://doi.org/10.1016/j.rse.2017.02.020>.
- [64] Y. Shi, K.K.-L. Lau, E. Ng, Developing street-level PM2.5 and PM10 land use regression models in high-density Hong Kong with urban morphological factors, *Environ. Sci. Technol.* 50 (2016) 8178–8187, <https://doi.org/10.1021/acs.est.6b01807>.
- [65] Y. Peng, R. Bucolieri, Z. Gao, W. Ding, Indices employed for the assessment of “urban outdoor ventilation” - a review, *Atmos. Environ.* 223 (2020), 117211, <https://doi.org/10.1016/j.atmosenv.2019.117211>.

- [66] J. Xiong, R. Yao, W. Wang, W. Yu, B. Li, A spatial-and-temporal-based method for rapid particle concentration estimations in an urban environment, *J. Clean. Prod.* 256 (2020), 120331, <https://doi.org/10.1016/j.jclepro.2020.120331>.
- [67] Y. Gao, J. Zhao, L. Han, Quantifying the nonlinear relationship between block morphology and the surrounding thermal environment using random forest method, *Sustain. Cities Soc.* 91 (2023), 104443, <https://doi.org/10.1016/j.scs.2023.104443>.
- [68] L. Han, J. Zhao, Y. Gao, Z. Gu, Prediction and evaluation of spatial distributions of ozone and urban heat island using a machine learning modified land use regression method, *Sustain. Cities Soc.* 78 (2022), 103643, <https://doi.org/10.1016/j.scs.2021.103643>.
- [69] Q. Wu, Z. Li, C. Yang, H. Li, L. Gong, F. Guo, On the scale effect of relationship identification between land surface temperature and 3D landscape pattern: the application of random forest, *Rem. Sens.* 14 (2022) 279, <https://doi.org/10.3390/rs14020279>.
- [70] X. Zhu, Y. Li, X. Wang, Machine learning prediction of biochar yield and carbon contents in biochar based on biomass characteristics and pyrolysis conditions, *Bioresour. Technol.* 288 (2019), 121527, <https://doi.org/10.1016/j.biortech.2019.121527>.
- [71] J. Chen, R. Chu, H. Wang, L. Zhang, X. Chen, Y. Du, Alleviating urban heat island effect using high-conductivity permeable concrete pavement, *J. Clean. Prod.* 237 (2019), 117722, <https://doi.org/10.1016/j.jclepro.2019.117722>.
- [72] X. Wei, F. Guan, X. Zhang, N. Van De Weghe, H. Huang, Integrating planar and vertical environmental features for modelling land surface temperature based on street view images and land cover data, *Build. Environ.* 235 (2023), 110231, <https://doi.org/10.1016/j.buildenv.2023.110231>.
- [73] W. Zhou, Y. Qian, X. Li, W. Li, L. Han, Relationships between land cover and the surface urban heat island: seasonal variability and effects of spatial and thematic resolution of land cover data on predicting land surface temperatures, *Landsc. Ecol.* 29 (2014) 153–167, <https://doi.org/10.1007/s10980-013-9950-5>.
- [74] R.A. Engel, A. Millard-Ball, V.K. Turner, Contributions of roads to surface temperature: evidence from Southern California, *Environ. Res. Commun.* 5 (2023), 015004, <https://doi.org/10.1088/2515-7620/acabb8>.
- [75] G. Guo, X. Zhou, Z. Wu, R. Xiao, Y. Chen, Characterizing the impact of urban morphology heterogeneity on land surface temperature in Guangzhou, China, *Environ. Model. Software* 84 (2016) 427–439, <https://doi.org/10.1016/j.envsoft.2016.06.021>.
- [76] W.-B. Wu, Z.-W. Yu, J. Ma, B. Zhao, Quantifying the influence of 2D and 3D urban morphology on the thermal environment across climatic zones, *Landsc. Urban Plann.* 226 (2022), 104499, <https://doi.org/10.1016/j.landurbplan.2022.104499>.
- [77] P. Luo, B. Yu, P. Li, P. Liang, Y. Liang, L. Yang, How 2D and 3D built environments impact urban surface temperature under extreme heat: a study in Chengdu, China, *Build. Environ.* 231 (2023), 110035, <https://doi.org/10.1016/j.buildenv.2023.110035>.
- [78] G. Kim, D. Cha, C. Song, H. Kim, Impacts of anthropogenic heat and building height on urban precipitation over the Seoul metropolitan area in regional climate modeling, *JGR Atmos.* 126 (2021), <https://doi.org/10.1029/2021JD035348>.
- [79] J. Allegriani, A wind tunnel study on three-dimensional buoyant flows in street canyons with different roof shapes and building lengths, *Build. Environ.* 143 (2018) 71–88, <https://doi.org/10.1016/j.buildenv.2018.06.056>.
- [80] E. Jamei, H.W. Chau, M. Seyedmohammadian, A. Stojcevski, Review on the cooling potential of green roofs in different climates, *Sci. Total Environ.* 791 (2021), 148407, <https://doi.org/10.1016/j.scitotenv.2021.148407>.
- [81] T. Susca, F. Zanghirella, L. Colasurdo, V. Del Fatto, Effect of green wall installation on urban heat island and building energy use: a climate-informed systematic literature review, *Renew. Sustain. Energy Rev.* 159 (2022), 112100, <https://doi.org/10.1016/j.rser.2022.112100>.
- [82] C.M. Nwakaire, C.C. Onn, S.P. Yap, C.W. Yuen, P.D. Onodagu, Urban Heat Island Studies with emphasis on urban pavements: a review, *Sustain. Cities Soc.* 63 (2020), 102476, <https://doi.org/10.1016/j.scs.2020.102476>.
- [83] M. Hendel, P. Gutierrez, M. Colombert, Y. Diab, L. Royon, Measuring the effects of urban heat island mitigation techniques in the field: application to the case of pavement-watering in Paris, *Urban Clim.* 16 (2016) 43–58, <https://doi.org/10.1016/j.uclim.2016.02.003>.
- [84] D. Xu, D. Zhou, Y. Wang, W. Xu, Y. Yang, Field measurement study on the impacts of urban spatial indicators on urban climate in a Chinese basin and static-wind city, *Build. Environ.* 147 (2019) 482–494, <https://doi.org/10.1016/j.buildenv.2018.10.042>.